A self-aligning upper-limb exoskeleton preserving natural shoulder movements: kinematic compatibility analysis

Jun Pan, *Member, IEEE*, Davide Astarita, Andrea Baldoni, Filippo Dell'Agnello, Simona Crea, *Member, IEEE*, Nicola Vitiello, *Member, IEEE*, Emilio Trigili, *Member, IEEE*

***Abstract*—NESM-γ is an upper-limb exoskeleton to train motor functions of post-stroke patients. Based on the kinesiology of the upper limb, the NESM-γ includes a four degrees-of-freedom (DOF) active kinematic chain for the shoulder and elbow, along with a passive chain for self-aligning robotic joint axes with the glenohumeral (GH) joint's center of rotation. The passive chain accounts for scapulohumeral rhythm and trunk rotations. To assess self-aligning performance, we analyzed the kinematic and electromyographic data of the shoulder in eight healthy subjects performing reaching tasks under three experimental conditions: moving without the exoskeleton (*baseline*), moving while wearing the exoskeleton with the passive DOFs properly functioning, i.e., unlocked (*human-in-the-loop(HIL)-unlocked*), and with the passive DOFs locked (*HIL-locked*). Comparison of *baseline* and *HIL-unlocked* conditions showed nearly unchanged anatomical movement patterns, with a root-mean-square error of shoulder angle lower than 5 deg and median deviations of the GH center of rotation below 20 mm. Peak muscle activations showed no significant differences. In contrast, the *HIL-locked* condition deviated significantly from the *baseline*, as observed by the trunk and GH trajectory deviations up to 50 mm, accompanied by increased peak muscle activations in the Deltoid and Upper Trapezius muscles. These findings highlight the need for kinematic solutions in shoulder exoskeletons that can accommodate the movements of the entire shoulder complex and trunk to achieve kinematic compatibility.**

***Index Terms*— rehabilitation robotics, upper-limb exoskeleton, kinematic design, experimental protocol.**

I. Introduction

Kinematic compatibility is a key requirement for the ergonomic design of a wearable robot, aiming to cover the physiological range of motion (ROM) while avoiding parasitic loads on the user caused by joint misalignments. Currently, two main approaches have been explored for addressing the issue of misalignment between the human and robot joint axes: 1) adoption of "soft" textiles or compliant elements and 2) inclusion of additional passive degrees of freedom (DOFs) into a rigid kinematic chain. Adopting textile, compliant elements results in "soft" [1], [2] or "flexible" [3]–[5] exoskeletons, specifically known as *exosuits*. These devices do not suffer from misalignment issues because they leverage human articulations to deliver movement assistance by means of pneumatic or cable-based systems. In addition, they usually deliver only a fraction of the biological joint torque and are employed for assisting patients with low or mild impairments. Conversely, rigid exoskeletons can deliver higher torques, but at the cost of more complex kinematic structures to ensure proper alignment between human and robot joints [6].

Achieving kinematic compatibility at the shoulder is an open challenge for rigid upper-limb exoskeletons due to the complicated biomechanics of the shoulder complex. The shoulder anatomy is commonly simplified by considering only three DOFs of the glenohumeral (GH) joint [7]–[11]. However, the combined movement of GH, scapulothoracic (ST), and sternoclavicular (SC) joints also occurs at the shoulder girdle (SG), including concomitant translational displacements of the center of rotation (CoR) of the GH joint, called elevation/depression (sE/D) and protraction/retraction (sP/R) [12]. Oversimplifying the anatomical DOFs in the kinematic design introduces misalignment between the human and robot joints, and it is likely to cause pain or even injury to the user.

Many studies have devoted efforts to designing shoulder exoskeletons with misalignment compensation strategies. Sui *et al*. used an articulated parallelogram resulting in one passive DOF (pDOF) for self-aligning during sE/D movement, while requiring a fixed trunk position relative to the shoulder joint base [13]. Since self-aligning measures adopting a single revolute DOF for mimicking the circular translation of the GH joint require the DOF to align precisely with the CoR of the sE/D movement, a translational DOF is included in series with the revolute one in the CLEVERarm device to mitigate this issue [14]. Other solutions have also tried to accommodate the misalignment during the sP/R movement. Harmony features an actuated parallelogram linkage to render a rotational axis for the sP/R [15]. In addition, a linear DOF is applied to align the axes

This work was supported by the EU Commission through the H2020 ReHyb project (Rehabilitation based on hybrid neuroprosthesis, Grant Agreement: 871767). Jun Pan was supported by the Key R&D Program of Zhejiang Province, China (grant 2019C03075), and by the China Scholarship Council (CSC) for his study at Scuola Superiore Sant'Anna, Pisa, Italy.

Corresponding authors: Jun Pan (jun.pan@ieee.org), Emilio Trigili (emilio.trigili@santannapisa.it).

J. Pan is with the College of Optical, Mechanical and Electrical Engineering, Zhejiang A&F University, Hangzhou 311300, Zhejiang, China. He was affiliated with Scuola Superiore Sant'Anna, Pisa.

D. Astarita, A. Baldoni, F. Dell'Agnello, S. Crea, N. Vitiello and E. Trigili are with The BioRobotics Institute, Scuola Superiore Sant'Anna, 56025 Pontedera, Italy, and with the Department of Excellence in Robotics & AI, Scuola Superiore Sant'Anna, 56127 Pisa, Italy.

S. Crea and N. Vitiello are also with IRCCS Fondazione Don Gnocchi, Florence, 50143, Italy. They have commercial interests in IUVO S.r.l., a spinoff company of Scuola Superiore Sant'Anna. Part of the IP protecting the NESM-γ has been licensed to IUVO S.r.l. for commercial exploitation.

of the human and robot vertically. MEDARM presents a shoulder girdle mechanism with two powered revolute joints intersecting at the user's SC joints [16]. ANYexo adopts a similar approach but assumes two different CoRs for the sE/D and sP/R movements [17]. NTUH-ARM adopts one powered linear DOF to align the human and robot axes vertically, while three powered revolute joints connected in series on the horizontal plane mobilize the GH joint both translationally and rotationally [18]. To enable arbitrary alignment in the 3-dimensional space, IntelliArm employs a mechanism of three translational DOFs, one placed vertically to compensate for the robot's gravity actively, and the other two sliding passively on the horizontal plane [19]. Finally, the first version of NESM adopted a self-aligning module for sE/D, sP/R, and trunk rotations based on passive revolute joints [20].

The advantage of using powered joints for mitigating misalignment issues is that they can actively counteract the force disturbances (e.g., gravity, inertia force, friction) that otherwise cause kinematic misalignment. Yet, the effectiveness of the compensation depends on a good model of the disturbances. Conversely, pDOFs have the advantages of low cost, compactness, and no control instability, but their self-aligning performance could deteriorate significantly when inertia force and friction increase.

Besides, most of the state-of-the-art upper-limb exoskeletons for rehabilitation assume a user trunk pose with a fixed position and orientation in the kinematic design [15], [17], [21]; in such platforms, safe and efficient delivery of the assistive torques can be ensured only if no major deviations of the trunk pose occur after the initial donning.

The potential benefits of self-aligning mechanisms are usually verified by means of theoretical models, and only a limited number of experimental studies have been carried out to assess quantitatively their effects on able-bodied participants. For example, the self-aligning mechanism of the ESA EXARM was evaluated by using objective metrics (i.e., interaction forces/torques), and subjective metrics via the NASA Task Load Index rating scale and a custom questionnaire for assessing user's comfort [22]. Authors in [23] included additional metrics such as knee kinematics and center of pressure to evaluate the self-aligning design of the Utah ExoKnee, by comparing the mechanism with the passive DOFs locked and unlocked, respectively [23]. In the Shoulder-Sidewinder, a comprehensive assessment at the physiological level was achieved by combining measurements of shoulder kinematics with electromyography (EMG) data [24].

This paper presents the kinematic design and experimental assessment of the kinematic compatibility of a novel exoskeleton, i.e., NEUROExos Shoulder-elbow Module - γ (NESM-γ, Fig. 1), for the physical motor-function training of post-stroke patients [25]. The kinematic chain has been designed to actively mobilize the GH joint and passively align the CoRs of the robot and human joints in the 3D space, also accounting for deviations of the user's trunk pose. Experimental verification with healthy subjects was carried out to assess the kinematic compatibility of the NESM-γ, by quantitatively characterizing the performance of the self-aligning mechanism and its effect on shoulder kinematics and muscle activations.

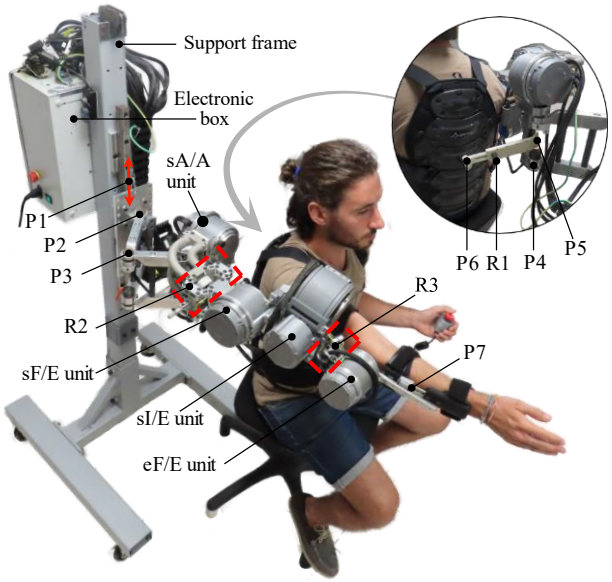

Fig. 1. Overview of the exoskeleton worn by a healthy subject.

The remainder of this article is structured as follows: Section II describes the system design of the NESM-γ, while Section III reports the experimental protocol. The results of the experiments are presented in Section IV. Results are discussed in Section V, and Section VI draws the conclusion.

II. System Design

The NESM-γ features a shoulder-elbow module to support GH abduction/adduction (sA/A), flexion/extension (sF/E), internal/external rotation (sI/E), and elbow flexion/extension (eF/E) movements via series-elastic actuators (SEAs) in a reaction force-sensing configuration [25]. Each SEA unit contains a brushless DC motor, a Harmonic Drive reducer, and a custom hollow torsional spring. Two absolute encoders measure the SEA torque (by sensing the spring deformation) and joint position, respectively. A passive chain allows the self-adaptability of the exoskeleton to the human movements at the CoR of the GH joint. The exoskeleton is mounted into a movable structure with a support column, which hosts the electronic box and a cable-pulley weight relief system connected to the first joint of the passive chain. A quick flipping mechanism using mechanical switches enables independent use on either the left or right arm. The weight of the shoulder-elbow module is 12.8 kg. Details of the mechatronic system have been reported in [25]. In this study, we focus on the kinematic analysis of the exoskeleton, starting from the functional requirements at the basis of its design.

A. Functional requirements

To ensure the comfort and ease of use of an exoskeleton, the kinematic design should allow the robot to adjust its pose and continuously adapt to human anatomy, without loading the musculoskeletal structure with undesired loads, and without restricting the ROM of the user. In a rehabilitation context, this purpose can be interpreted as three kinematic design requirements: 1) the robot must replicate the mobility of the

TABLE I
DH parameters of the shoulder-elbow module

Module	Joint	a_{j-1} (mm)	α_{j-1}(deg)	d_j (mm)	θ_j (deg)
Passive chain	S-P1	0	0	$p_1 + 828.3$	90
	P1-P2	89	0	0	θ_{p2}
	P2-P3	200	0	0	θ_{p3}
	P3-P4	200	0	0	θ_{p4}
	P4-O_{GH}	r_2	0	261	-90
Active module	O_{GH}-J1	0	-90	0	$\theta_1 + 180$
	J1-J2	0	90	0	θ_2
	J2-Jv	0	-90	r_3	$\theta_3/2$
	Jv-J3	0	0	0	$\theta_3/2$
	J3-J4	0	90	0	θ_4
	J4-P7	0	-90	$p_7 + 150.5$	0

Note. p_1 is the translation of the vertical DOF P1; p_2~p_4 are joint angles of the horizontal pDOFs P2~P4; θ_1~θ_4 are the joint angles of the actuation units sA/A, sF/E, sI/E and eF/F; r_2 is the distance between the joint P4 and Joint O along the *z*-axis of P4 determined by the regulation DOF R2; r_3 is the distance between the joint J2 and Jv along the *x*-axis of Jv set by the regulation DOF R3; p_7 is the translation of the pDOF P7.

anatomical joints of the upper limb to guarantee sufficient workspace for rehabilitation training; 2) the robot should not require the user to maintain a fixed relative position to exempt the therapist from arduous efforts during the donning procedure, and to permit natural deviation of the user's trunk from the initial pose for the sake of comfort: 3) the human and robot axes should be properly aligned such that the mutual movement synergy and power transmission occur as desired.

B. *Kinematic configuration*

Fig. 2 illustrates the kinematic chain of the platform, which comprises three branches.

The first includes the active shoulder-elbow module, in which: the active shoulder joints (sA/A, sF/E, and sI/E) have three intersecting axes aligned with the center of the GH joint (O_{GH}); the sI/E joint is modeled with a virtual joint Jv and implements a differential mechanism, as described in [25]; the eF/E joint is simplified as a revolute joint with a translational DOF for alignment (pDOF P7); regulations R2 and R3 allow for manual adjustments for different acromion and humerus lengths. The active module has been designed to cover sufficient workspace for rehabilitation training (1st functional requirement). The second branch comprises a passive chain (P1-P2-P3-P4) between the base of the platform and the active module to allow the exoskeleton and the user to deviate from the base (2nd functional requirement). Finally, another passive kinematic chain (P5-R1-P6) coupling the shoulder complex in a closed loop facilitates instantaneous joint alignment between the human and robot (3rd functional requirement).

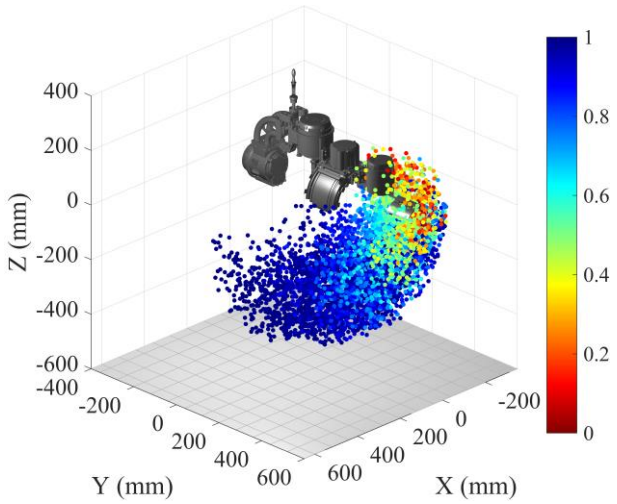

Fig. 3. Workspace and manipulability of the shoulder-elbow module.

The kinematics was modeled based on the modified Denavit–Hartenberg (DH) convention, with a reference zero-configuration shown in Fig. 2. DH parameters are summarized in TABLE I. Considering the frame {W} at the end of the forearm link, the workspace of the active shoulder-elbow module was estimated via the Monte Carlo method, by spanning the ROM of the four actuation units (sA/A [0:90] deg, sF/E [0:90] deg, sI/E [-88:28] deg, eF/E [-120:0] deg) and the stroke of the slider p_7 ([0,85] mm) with 5000 uniformly distributed random steps. The value of r_3 was 308.8 mm. For each combination, the manipulability index w $\in$ [0,1] was calculated as $w = \sqrt{det\,(JJ^T)}$, where J is the Jacobian matrix and w is normalized to its maximum value [26]. A value of 0 indicates a kinematic singularity, thus higher values (closer to 1) preferred. The results of the simulation are shown in Fig. 3.

C. *pDOFs for shoulder elevation/depression*

Fig. 4a illustrates the kinematic coupling when the user wears the robot. In the rest of the paper, we will refer to this condition as *human-in-the-loop* (HIL). The kinematic analysis of our chain of pDOFs (P1-P2-P3-P4) can be decoupled into one for the vertical direction and another for horizontal movement. Since P1 is the only vertical DOF interacting with the shoulder, the vertical position of P1 (d_{p1}) and the one of O_{GH} (z_{GH}) is equal when placing the coordinate frame of P1 at the height of the sA/A joint at the zero-configuration pose, i.e., $d_{p1_0} = z_{GH_0}$.

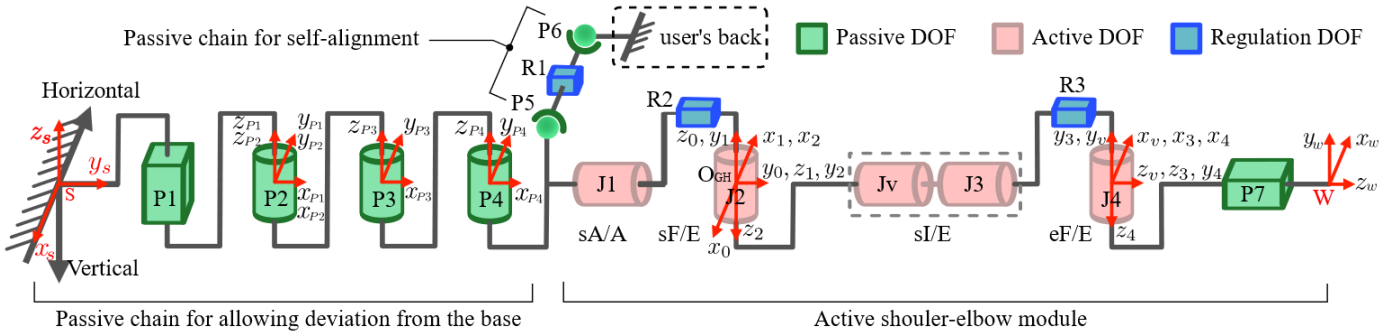

Fig. 2. Kinematic chain of the exoskeleton represented with a zero-configuration based on the modified DH convention.

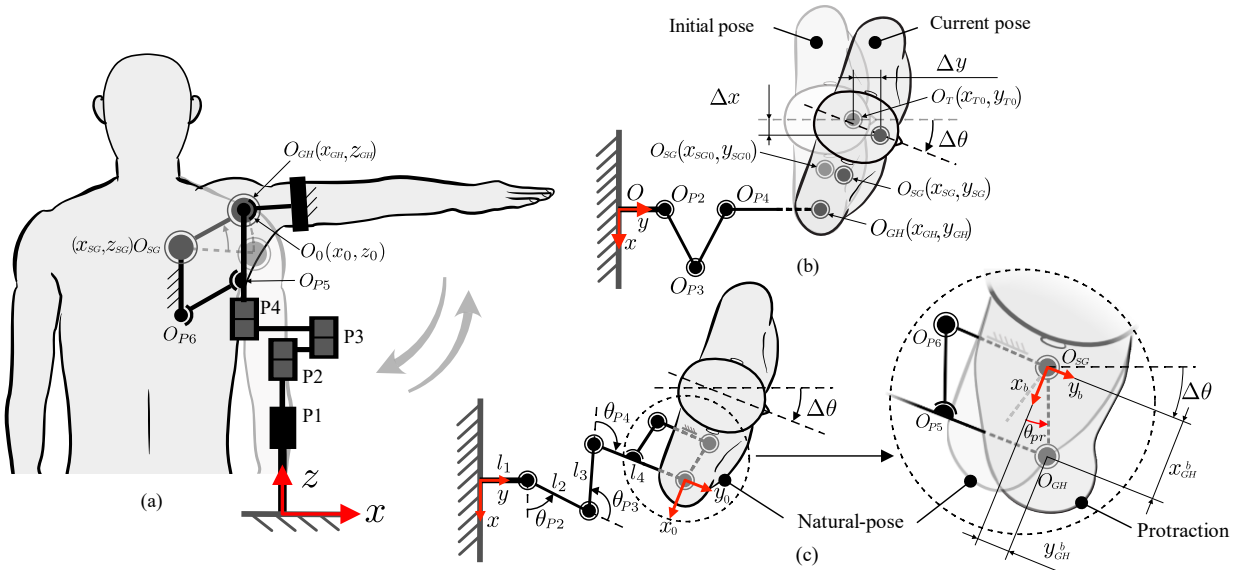

Fig. 4. (a) CoR tracking of the GH joint on the vertical plane. (b) CoR tracking of the GH joint on the horizontal plane. (c) Orientational alignment provided by the closed kinematic chain with the user's trunk. Acronyms list. GH: glenohumeral joint; SG: shoulder girdle P: passive joint.

Let us define (x_{SG}, y_{SG}, z_{SG}) as the position of O_{SG} in the world frame {O}. Given a human-robot alignment at O_{GH}, we have:

$$d_{P1} = z_{GH_0} + z_{GH}^b, \tag{1}$$

where z_{SG} can be considered constant due to the neglectable change of trunk position along the vertical direction, and z_{GH}^b is the vertical displacement of O_{GH} with respect to O_{SG}. Equation (1) indicates that the translational movement of joint P_1 copes with the sE/D movement.

D. pDOFs for shoulder protraction/retraction

Considering the horizontal pDOFs chain in Fig. 4b, a trunk rotation of $\Delta\theta$ around O_{GH} would result in a trunk deviation of $(\Delta x, \Delta y)$ from the initial pose and a change in the CoR of the shoulder girdle (x_{SG}, y_{SG}) according to the following equation:

$$\begin{cases} (x_{T0} + \Delta x - x_{SG})^2 + \left(y_{T0} + \Delta y - y_{SG}\right)^2 = \\ \quad (x_{T0} - x_{SG0})^2 + \left(y_{T0} - y_{SG0}\right)^2 \\ atan\left(\dfrac{y_{T0} + \Delta y - y_{SG}}{x_{T0} + \Delta x - x_{SG}}\right) - atan\left(\dfrac{y_{T0} - y_{SG0}}{x_{T0} - x_{SG0}}\right) = \Delta\theta \end{cases}, \tag{2}$$

where (x_{SG0}, y_{SG0}) is the O_{SG} position in the initial pose, and (x_{T0}, y_{T0}) is the initial trunk position O_T, assuming that the distance between points O_T and O_{SG} does not change during the movement. This model shows how trunk rotation changes the CoR position of the shoulder girdle.

Let us define (x_{GH}^b, y_{GH}^b) as the position in the local horizontal frame of O_{SG} (Fig. 4c). Based on the anatomical constraints, the position of O_{GH} can be expressed as:

$$\begin{cases} x_{GH} = x_{SG} + x_{GH}^b cos\Delta\theta + y_{GH}^b sin\Delta\theta \\ y_{GH} = y_{SG} + x_{GH}^b sin\Delta\theta + y_{GH}^b cos\Delta\theta \end{cases} \tag{3}$$

where $x_{GH}^b = r_h cos\theta_{pr}$, $y_{GH}^b = r_h sin\theta_{pr}$, r_h is the distance between O_{GH} and O_{SG}, and θ_{pr} is the protraction/retraction angle.

Combining (2) and (3), the horizontal position of O_{GH} can be formalized as:

$$(x_{GH}, y_{GH}) = \big(f(u), g(u)\big), \tag{4}$$

where $u = (\Delta x, \Delta y, \Delta\theta, \theta_{pr})$. This equation shows that the position of the CoR of the GH joint is a function of the trunk deviation and shoulder girdle movement.

Furthermore, for the coupled human-robot kinematic chain, constraints on the GH position (x_{GH}, y_{GH}) result in:

$$\begin{cases} x_{GH} = l_2 cos\theta_{p2} + l_3 cos(\theta_{p2} + \theta_{p3}) \\ \quad + l_4 cos(\theta_{p2} + \theta_{p3} + \theta_{p4}) \\ y_{GH} = l_1 + l_2 sin\theta_{p2} + l_3 sin(\theta_{p2} + \theta_{p3}) \\ \quad + l_4 sin(\theta_{p2} + \theta_{p3} + \theta_{p4}) \end{cases}, \tag{5}$$

where $\theta_{p2}, \theta_{p3}, \theta_{p4}$ are rotation angles of joints P2, P3, and P4, and l_1, l_2, l_3, l_4 are the lengths of the links connecting the pDOFs. Note that O_{GH} is regarded as having a fixed position relative to O_{P4} once the user dons the robot, and l_4 can be set according to the user's body size by manually regulating R2.

Equations (4) and (5) demonstrate that the horizontal pDOFs can accommodate the trunk deviation $(\Delta x, \Delta y, \Delta\theta)$ and shoulder girdle movement (θ_{pr}) with an instantaneous pose $(\theta_{P2}, \theta_{P3}, \theta_{P4})$.

However, since (x_{GH}, y_{GH}) is a 2-order kinematic constraint applied on a 3-DOF kinematic model, the pose of the human-robot kinematic chain is still undetermined because of the arbitrary rotation at O_{GH} in the horizontal plane, which leads to undesired or floating orientations of the sA/A joint. This problem is illustrated in Fig. 4b: the user's sagittal plane becomes misaligned with the orientation of the sA/A joint (pointing from P_4 to O_{GH}) after the trunk rotates by $\Delta\theta$, which causes incorrect joint-to-joint power transmission between human and robot, thus eliciting an uncomfortable human-robot interaction.

E. pDOFs for orientational alignment

To cope with the undetermined kinematics discussed above,

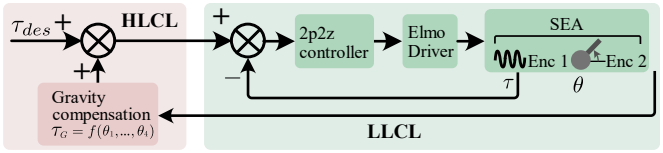

Fig. 5. Control architecture of the NESM-γ.

we introduced an additional kinematic chain (P_5-R_1-P_6) to pose constraints to the orientation of the sA/A axis. By tuning $R1$ and $R2$ and attaching O_{P6} at a point on the back of the user that aligns with O_{SG} in the sagittal plane, the robotic joints and shoulder anatomy form a closed kinematic chain ($O_{P5} - O_{P6} - O_{SG} - O_{GH}$) that behaves as a parallelogram (Fig. 4c). Consequently, $O_{P5} - O_{GH}$ will move parallel with $O_{P6} - O_{SG}$ during sP/R movement. As such, the first joint of the active module, i.e., the sA/A unit, will be oriented parallel with the user's trunk, facilitating precise power transmission.

F. Control Architecture

The control architecture of the NESM-γ features a high-level control layer (HLCL) and a low-level control layer (LLCL), see Fig. 5. On the LLCL, a 2-pole-2-zero (2p2z) torque controller determines the required current for the motor driver, based on the error between the measured (τ) and reference torque [25]. The HLCL computes the reference torque by adding a pose-dependent feed-forward gravity compensation term (τ_G) to the desired human-robot interaction torque (τ_{des}) [25]. In the so-called *transparent mode*, τ_{des} is set equal to zero.

III. Experimental Evaluation

An experimental session with eight healthy participants was conducted to verify the kinematic compatibility of the NESM-γ with HIL. To evaluate the effect of the exoskeleton on the users' shoulder kinematics and muscle activations, we compared shoulder movements under three different conditions, i.e., without wearing the exoskeleton (*baseline*), wearing the exoskeleton with the pDOFs locked (*HIL-locked*), and wearing the exoskeleton with the pDOFs free to move (*HIL-unlocked*).

A. Participants

Eight healthy male subjects (age: 28.9±3.6 yrs, height: 180±6.7 cm, weight: 72.6±8.6 kg, Body Mass Index: 22.4±2.3 kg/m^2, all right-handed) volunteered to participate in the study. Participants were included in the study if they were between 18 and 70 years old, and if they had no cognitive disorders or physical conditions that could alter normal shoulder functions (e.g., recent sprains or injuries). The sample size was chosen in line with similar studies in the literature [23]. The study was approved by the local Institutional Review Board (approval n. 35/2021), and experiments were conducted at The BioRobotics Institute of Scuola Superiore Sant'Anna (Pontedera, Pisa, Italy), following the principles stated in the Declaration of Helsinki. All participants signed informed consent.

B. Experimental setup

The setup is illustrated in Fig. 6a. Robotic data, i.e., joint angles, were recorded by the encoders of the sensorized joints at 100 Hz and visualized online on a graphic user interface, for the convenience of the experimenter's evaluation. Kinematic data of the human body were acquired at 40 Hz by using the Aurora electromagnetic field (EMF) tracker (Northern Digital Inc., Waterloo, Canada, model AA138), which can track the position and orientation of magnetic sensors within a defined volume when varying magnetic fields are applied using a signal generator box. The EMG signals were collected to analyze muscle activations using pre-gelled bipolar Ag/AgCl surface electrodes (Pirrone & Co., Milan, Italy) and acquired by BTS FREEEMG 1000 (BTS Bioengineering, Milan, Italy), with a sampling frequency of 1 kHz. Robot and EMG data were synchronized via a wired connection of the digital I/O ports of the two devices. Due to the lack of I/O ports on the Aurora system, kinematic data were synchronized with the robot signals through an abrupt movement performed by the subject at the beginning of the trial, resulting in a distinguishable peak signal in both systems. Two visual markers clamped to two vertical rods were placed posteriorly and laterally to guarantee the same test movements' ROMs.

C. Preparation

1) Sensor placement: Fig. 6b specifies the placement scheme of both the EMF and EMG sensors. The EMF sensors were placed on the SC joint, upper arm (UA), and the acromion (AM) to track the position and orientation of the subject's upper limb and trunk. The EMG sensors were placed in pairs on five

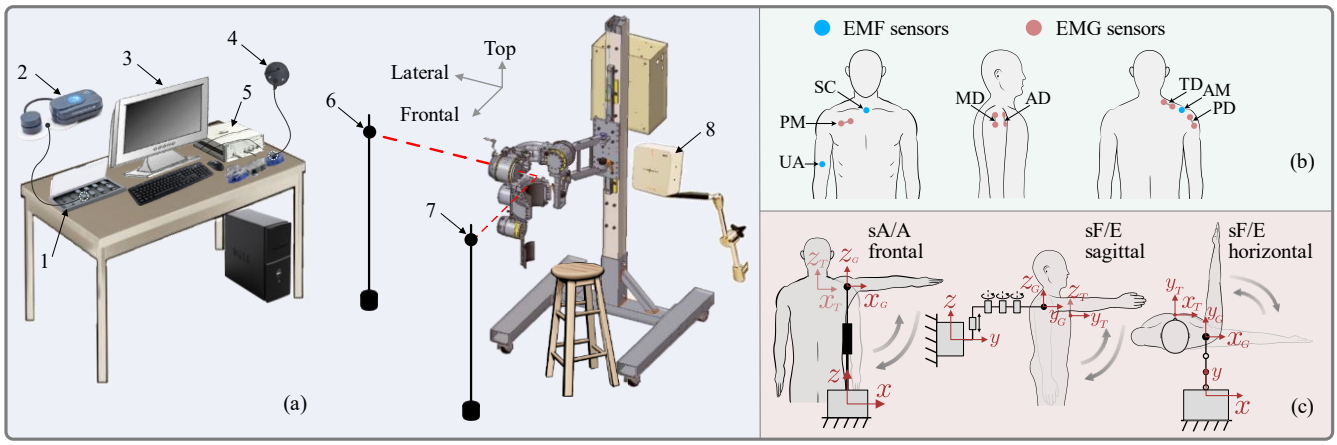

Fig. 6. (a) Experimental setup: 1 – EMG electrode, 2 – BTS FREEEMG 1000, 3 – Graphical User Interface, 4 – EMF sensor, 5 – EMF tracker, 6 – lateral visual marker, 7 – anterior visual marker, 8 – EMF signal generator. (b) Sensor placement scheme. (c) Experimental tasks.

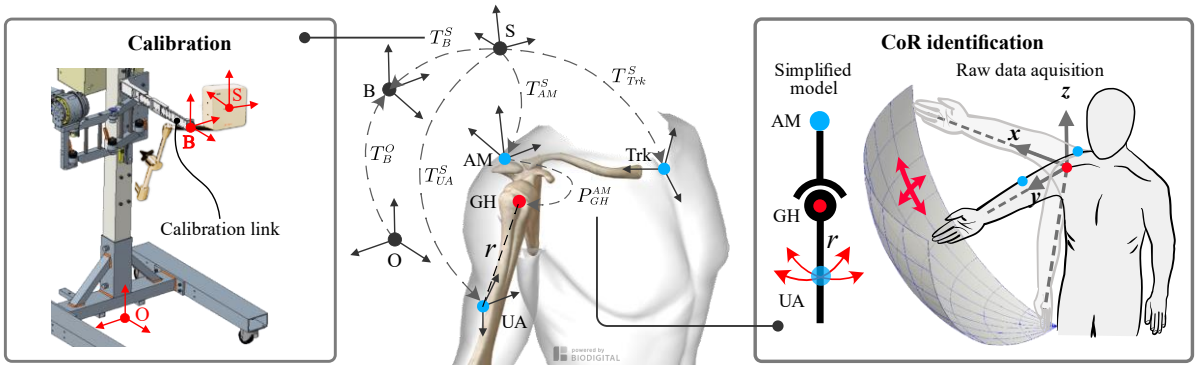

(a) (b) (c)

Fig. 7. (a) Position calibration of the Aurora system. (b) Transformation matrices between frames on the robot and human (Adapted from BioDigital - www.biodigital.com – with permission). (c) CoR identification of the GH joint.

muscles: trapezius descendens (TD), medial deltoid (MD), anterior deltoid (AD), posterior deltoid (PD), and pectoralis major (PM), following SENIAM guidelines [27]. The activity of TD reflects the movement of the scapulohumeral rhythm. MD is mostly involved during sA/A movements in the frontal plane. AD, PD, and PM are mostly activated during sF/E movements in the sagittal and horizontal planes.

2) Maximum voluntary contraction (MVC) test: Three 5-second MVCs for each muscle were recorded to normalize the EMG signals. The MVC value was computed as the global maximum of the three repetitions.

3) Aurora position calibration: To convert the trajectory expressed in the frame of the EMF signal generator {S} into the global frame of the robot {O}, a calibration link was temporarily fixed to the P1 slider of the robot in the zero position, and one EMF sensor was attached to the distal end {B} (Fig. 7a). The position of the EMF sensor was recorded, and the link was removed afterward. The calibration determines the transformation matrix of frame {B} into frame {S}, i.e. T_B^S (Fig. 7b), which allows for correlation between the positions of the robot, the Aurora system, and the human subject. The position of the trunk in the global frame {O}, i.e., P_{Trk}, was obtained by:

$$\begin{cases} T_{Trk}^O &= T_B^O (T_B^S)^{-1} T_{Trk}^S \\ P_{Trk} &= T_{Trk}^O(1{:}3,4) \end{cases}, \quad (6)$$

and the position of O_{GH}, i.e., P_{GH} by:

$$\begin{cases} P_{GH}^O &= T_B^O (T_B^S)^{-1} T_{AM}^S P_{GH}^{AM} \\ P_{GH} &= P_{GH}^O(1{:}3,1) \end{cases}, \quad (7)$$

where P_{GH}^{AM} is the position of the CoR of the GH joint with respect to the frame {AM}. T_B^O was determined from CAD drawing, given the known position of the calibration link. T_{AM}^S, T_{UA}^S, and T_{Trk}^S were obtained from the data recorded by the Aurora system after converting the quaternions into rotational matrices and integrating the translational components (Fig. 7b).

4) CoR identification of the GH joint (O_{GH}): O_{GH} approximates a point with a constant offset from the AM [28] and P_{GH}^{AM} can be obtained through an identification procedure. The UA position expressed in the frame {AM}, i.e., P_{UA}^{AM}, can be calculated by:

$$\begin{cases} T_{UA}^{AM} &= (T_{AM}^S)^{-1} T_{UA}^S \\ P_{UA}^{AM} &= T_{UA}^{AM}(1{:}3,4) \end{cases}, \quad (8)$$

For the identification, each subject was asked to fully extend the elbow and span the eighth of a spherical surface with vertical and horizontal back-and-forth movements (Fig. 7c). In this condition, UA describes a circular trajectory with radius r about O_{GH}, and the identified CoR position of the trajectory P_{UA}^{AM} equals P_{GH}^{AM}. The least-square error method was applied to estimate P_{GH}^{AM}, i.e.:

$$\begin{cases} e_i(x_{GH}^{AM}, y_{GH}^{AM}, Z_{GH}^{AM}, r) = \\ \quad (x_i - x_{GH}^{AM})^2 + (y_i - y_{GH}^{AM})^2 + (z_i - z_{GH}^{AM})^2 - r^2 \\ E(x_{GH}^{AM}, y_{GH}^{AM}, Z_{GH}^{AM}, r) = \sum_{i=1}^{N} e_i(x_{GH}^{AM}, y_{GH}^{AM}, Z_{GH}^{AM}, r)^2 \\ \quad min\big(E(x_{GH}^{AM}, y_{GH}^{AM}, Z_{GH}^{AM}, r)\big) \end{cases}, \quad (9)$$

where $P_{GH}^{AM} = (x_{GH}^{AM}, y_{GH}^{AM}, Z_{GH}^{AM})$, $(P_{UA}^{AM})_i = (x_i, y_i, z_i)$, i is the sample index, N is the total number of samples, r is the estimated radius, e_i is the squared distance between sample i and O_{GH}, and E is the sum of all e_i, i.e., the optimization goal.

D. Experimental Tasks

Three primitive movements of the shoulder were selected to assess the effect of the robot kinematic chain on the anatomical trajectories and muscle activations (Fig. 6c): shoulder abduction/adduction in the frontal plane (*sA/A frontal*), shoulder flexion/extension in the sagittal plane (*sF/E sagittal*), and shoulder horizontal flexion/extension (*sF/E horizontal*).

After donning the robot with the help of the experimenter, the subjects were asked to perform the first three trials (one for each primitive movement) in the *HIL-unlocked* condition, followed by three trials in the *HIL-locked* condition. Finally, the robot was doffed, and three *baseline* trials were performed. In each trial, the subject was instructed to keep the trunk still while performing the movement back and forth naturally for 12 repetitions, following a metronome at 24 beats per minute (bpm). After each trial, the subject took a 3-minute rest.

E. Data processing

Data analysis was conducted in MATLAB 2022 (MathWorks, USA) with custom routines.

1) Limb angle measurement: The limb angle θ_{lb}, describing the 1-DOF movement of the shoulder (Fig. 6c), was computed for data segmentation. For the baseline trials, the EMF sensor attached to UA was used to track θ_{lb}, based on the following

equation:

$$\theta_{lb} = \begin{cases} \pi/2 - \Delta\theta_{lb}, & \text{sA/A frontal and sF/E sagittal} \\ \Delta\theta_{lb}, & \text{sF/E horizontal} \end{cases}, \quad (10)$$

where:

$$\begin{cases} \Delta\theta_{lb} &= 2 * acos\,(\boldsymbol{q}_{0i}(1)) \\ \boldsymbol{q}_{0i} &= \boldsymbol{q}_0^{-1}\boldsymbol{q}_i \end{cases}, \quad (11)$$

and $\boldsymbol{q}_0$ is the quaternion at the zero pose, $\boldsymbol{q}_i$ is the quaternion at an instantaneous moment. In contrast, during HIL trials, θ_{lb} was obtained directly from the robotic joint angles' measurement:

$$\theta_{lb} = \begin{cases} \pi/2 - \theta_1, & \text{sA/A frontal} \\ \pi/2 - \theta_2, & \text{sF/E sagittal} \\ \pi/2 - \theta_2 + \theta_{p2} + \theta_{p3} + \theta_{p4}, & \text{sF/E horizontal} \end{cases}, \quad (12)$$

where θ_1 is sA/A angle, θ_2 is sF/E angle, and θ_{p2}, θ_{p3}, and θ_{p4} are the angles of the passive joints P2, P3, and P4.

2) Kinematic data (robot and EMF tracker): Data segmentation was performed by finding the maximum and minimum peaks of the limb angle profile for the last ten repetitions in each trial. Further, the mean and standard deviation of θ_{lb}, P_{Trk}, and P_{GH} over all the data cycles were calculated. To account for variations of the initial sitting position of the subject between trials, the trajectory data were offset with the first point of the mean trajectory, thus obtaining the trajectory variations, i.e., ΔP_{Trk} and ΔP_{GH}. Besides, the Root Mean Square Errors (RMSEs) of θ_{lb}, ΔP_{Trk} and ΔP_{GH} between the HIL conditions and the baseline were calculated. For the evaluation of the group performance, median and interquartile ranges (25th and 75th) were also calculated.

3) EMG data: EMG signals were bandpass filtered with a 2nd order Butterworth filter (frequency range: 20-450 Hz) and a zero-lag, second-order, 50 Hz notch filter. Then, the EMG signals were rectified, and the envelope was obtained with a zero-lag 100-ms moving average filter. The envelope amplitude was normalized by the corresponding MVC value for each muscle, and the mean and standard deviation profiles were calculated over the last 10 data cycles. The top 5% of the normalized EMG values of each cycle were averaged to compute the peak EMG. Then, the across-subject average was calculated (median and interquartile range of 25th and 75th).

F. Statistical Analysis

Statistical analysis with significance level $\alpha < 0.05$ was conducted to assess differences in the kinematic and EMG metrics among the three conditions. The Shapiro-Wilk test was used to check the data normality. For kinematic metrics (two conditions), if normality held, the paired-sample t-test was used to assess the significance of the difference. Otherwise, the pairwise Wilcoxon signed-rank test was performed. For EMG metrics (three conditions), parametric one-way repeated measures analysis of variance (rANOVA) was used to check across-condition differences of the normally distributed data, and then the Bonferroni method was applied to conduct the *post-hoc* comparisons. If the data was not normally distributed, Friedman's test was used to check the cross-condition difference, and the Wilcoxon test was used to perform the *post-hoc* comparisons.

IV. Results

A. Kinematic performance

One representative subject: The segmented data of θ_{lb}, ΔP_{Trk}, and ΔP_{GH} of one representative subject are visualized in Fig. 8. The overlapping limb angle profiles show consistent movements across all test conditions, and the deviations between the trajectory plots reflect the kinematic effect due to the change in test conditions. The plots show a different kinematic pattern of the *HIL-locked* condition with respect to the baseline. In contrast, the trajectories of the *HIL-unlocked* condition remain close to the baseline in most cases. Specifically, for the sA/A frontal movement, the significant deviation (median of 19.8 mm in the z-direction) of the CoR trajectory of the GH joint (ΔP_{GH}) was caused by the reduced

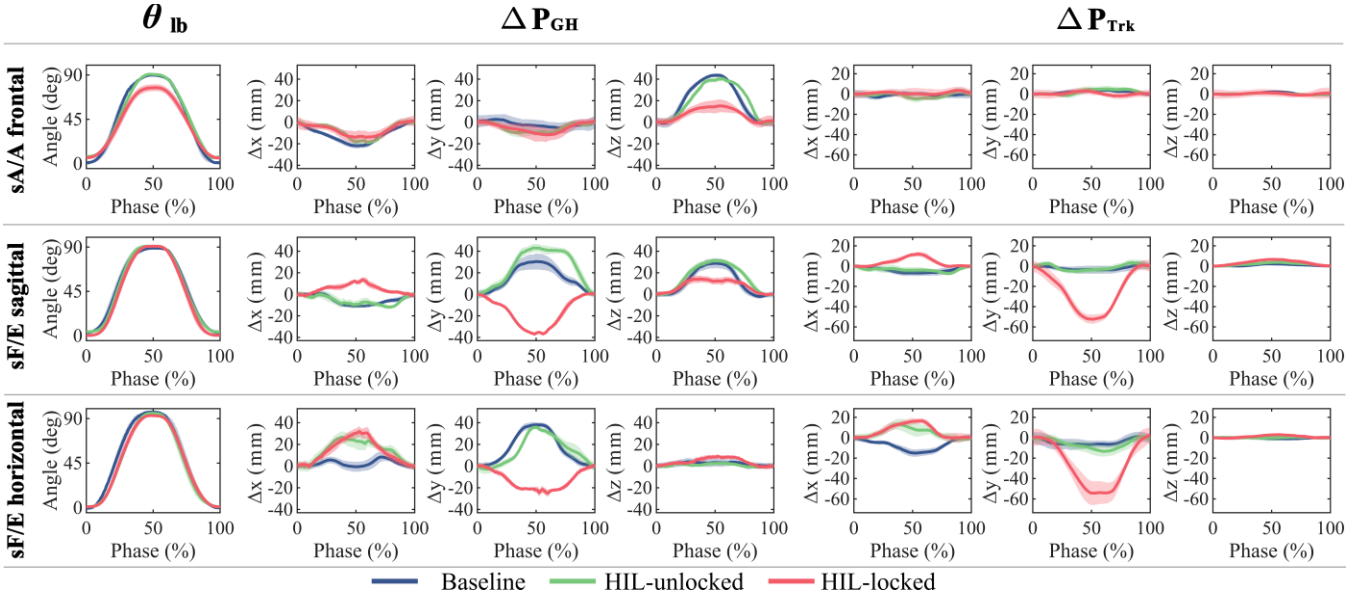

Fig. 8. Kinematic data of one representative subject, with mean (solid profiles) and standard deviations (shaded areas). θ_{lb} is the shoulder angle during the 1-DOF movement, ΔP_{GH} and ΔP_{Trk} represents respectively the 3D trajectories of the glenohumeral joint's center of rotation and trunk, de-offset from the initial value.

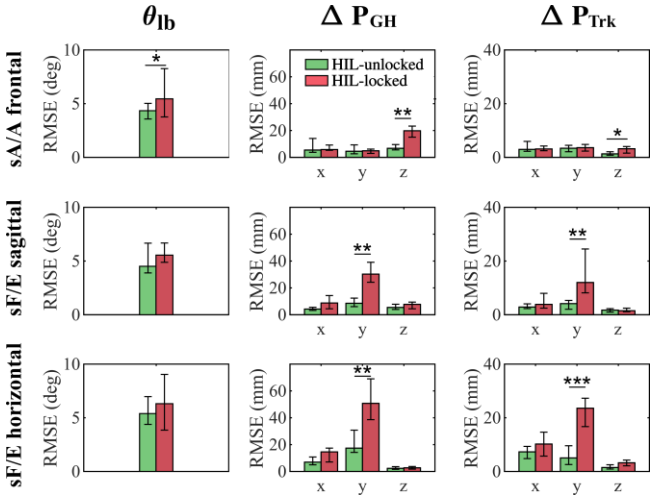

Fig. 9. Statistics of kinematic data. *: $p \leq 0.05$; **: $p \leq 0.01$; ***: $p \leq 0.001$

vertical translation in the z-direction. The deviations from the baseline for the sF/E sagittal movement and the sF/E horizontal movement were mainly on the y-axis components, with median ΔP_{GH_y} deviations of 30.3 mm and 50.8 mm, and ΔP_{Trk_y} deviations of 12 mm and 23.6 mm, for the two movements respectively.

Group results: Fig. 9 plots the RMSEs of the trajectories in HIL conditions relative to the baseline across all subjects. For the sA/A frontal movement, the RMSE of θ_{lb} in the *HIL-locked* condition shows a significant increase of 25.3% (1.1 deg, $p = 0.0282$) with respect to the *HIL-unlocked* condition. All three movements have an RMSE of the limb angle θ_{lb} of about 5 deg. Besides, the RMSEs of the z-component of ΔP_{GH} and ΔP_{Trk} under *HIL-unlocked* and *HIL-locked* conditions show significant statistical differences ($p = 0.0078$ and $p = 0.0157$), with the increase of ΔP_{GH} by 193.3% (13.1 mm) and ΔP_{Trk} by 145.8% (1.9 mm). Apart from the RMSE of the z-component of ΔP_{GH} reaching almost 20 mm, other RMSE medians are well below 10 mm. For the other two movements, RMSEs of y-components of both ΔP_{GH} and ΔP_{Trk} show significant differences under two conditions ($p < 0.01$), with an increase of ΔP_{GH} by 255% (21.8 mm) and ΔP_{Trk} by 190% (7.9 mm) for the sF/E sagittal movement, and the increase of ΔP_{GH} by 191.7% (33.3 mm) and ΔP_{Trk} by 366.7% (18.5 mm) for the sF/E horizontal movement, while the RMSEs of x- and z-component are similar and below 10 mm.

B. *Muscular activity*

One representative subject: Fig. 10a illustrates the muscular activities of the six muscles of all three movements for a representative subject. For the sA/A frontal movement, TD, PD, and PM muscles achieved higher peak activations in the *HIL-locked* condition than the *HIL-unlocked* condition, while the amplitudes of EMG peaks of MD and AD muscles rose from *baseline* to the *HIL-unlocked* condition. For the sF/E sagittal movement, the different conditions seem not to affect the EMG profiles significantly. Regarding the sF/E horizontal movement, the MD and PD muscles both have an EMG peak before the end of the cycle, where the peaks increased from *baseline*, *HIL-unlocked* to *HIL-unlocked* condition.

Group results: Fig. 10b reports the peak EMG amplitudes of the six muscles of all three movements under different conditions across all subjects. For the sA/A frontal movement, the MD and PD muscles show increased EMG activity in *HIL-unlocked* trials compared with *baseline* by 29.3% (p=0.1075) and 62.8% (p=0.0176), respectively, while the TD muscle exhibits increased EMG activity under *HIL-locked* condition over *HIL-unlocked* test by 52.8% (p=0.023). The EMG amplitudes of the TD, MD, and PD muscles increased significantly from *baseline* to the *HIL-locked* condition by 45.6% (p=0.0207), 36.6% (p=0.0468), and 62.4% (p=0.0502), respectively. However, no significant difference exists between the EMG activities of different conditions for the sF/E sagittal movement. Regarding the sF/E horizontal movement, the PD muscle exhibits an increased EMG by 86.2% (p=0.0051) in the *HIL-unlocked* trials compared with the *baseline*, and an increased EMG by 105.1% (p=0.0025) in the *HIL-locked* trials over the *baseline*; besides, the MD and PD muscles achieved higher activations by 30% (p=0.0211) and 10% (p=0.0119) of the *HIL-locked* condition over the *HIL-unlocked* test.

V. Discussion

A. *Assessment of the effects on the kinematics*

Kinematic data in the *baseline* condition confirmed the vertical GH joint translation of the natural shoulder adduction/abduction movement brought by the scapulohumeral rhythm, and the horizontal translation due to protraction/retraction concomitant with the natural flexion/extension movement on the horizontal plane. Statistical

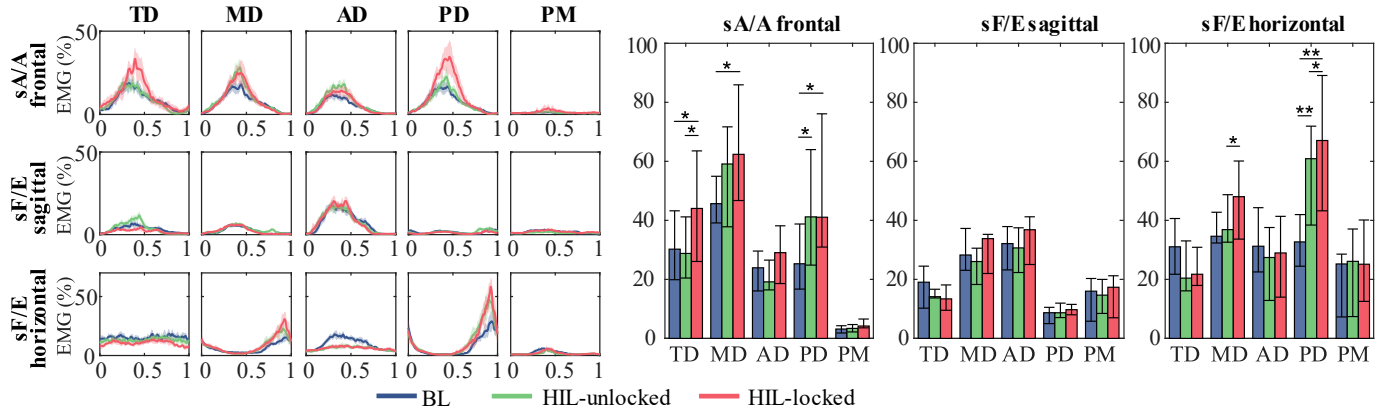

Fig. 10. EMG Data. (a) Data of one representative subject. (b) Statistics. *: $p \leq 0.05$; **: $p \leq 0.01$; ***: $p \leq 0.001$

analysis of the kinematic data showed a significant difference in ROMs between *HIL-unlocked* and *HIL-locked* conditions across all subjects for the sA/A frontal movement, but not for the other movements. Indeed, constraining the vertical translation of the GH joint resulted in a limited ROM due to discomfort experienced by the users for high elevation angles. The *HIL-unlocked* condition deviated from the *baseline* by an RMSE lower than 5°, revealing a good match of the ROM of the test movements.

For the *HIL-unlocked* condition, the median RMSE of ΔP_{GH} and ΔP_{Trk} along all axes of all three movements were below 10 mm, meaning that the passive kinematic chain is effective in preserving the shoulder and trunk movement patterns. For the *HIL-locked* condition, the natural movement pattern seemed to have been significantly modified during all three movements. Specifically, the RMSE of ΔP_{GH} and ΔP_{Trk} along the z-axis increased for SA/A frontal movement versus the *HIL-unlocked* condition. This was caused by the locked vertical passive DOF inhibiting natural scapulohumeral rhythm, thus impeding the translation of the GH joint along the z-axis. The RMSE of ΔP_{Trk} was relatively small (lower than 5 mm), which is reasonable as the subjects always kept their trunk upright during the experiments. Regarding the sF/E sagittal movement, the RMSEs of ΔP_{GH} and ΔP_{Trk} in the *HIL-locked* test were much higher than in the *HIL-unlocked* test along the y-axis (anterior direction), demonstrating that the natural movement pattern was significantly altered due to the locked horizontal passive DOFs, which prevented the robot from tracking the GH joint. As expected, the locked condition applied a kinematic constraint that held the GH joint at a constant position.

In contrast, the unlocked passive kinematic chain enabled the GH joint to translate horizontally, following the natural movement pattern, as shown by the significant difference of RMSEs of ΔP_{GH} between the two *HIL* conditions. Since the GH joint was locked, a compensatory posterior translation of the trunk was elicited to accomplish sF/E sagittal movement, as shown in the kinematic data of the representative subject (Fig. 8). Such a compensatory behavior explains the significant gain of the RMSE of ΔP_{Trk} along the y-axis in the *HIL-locked* tests over the *baseline*. As expected, similar results applied to the sF/E horizontal movement since the accompanying shoulder protraction/retraction also exists in this movement. However, the greater RMSEs of the sF/E horizontal movement compared with the sF/E sagittal movement shows that the former movement was more affected by the exoskeleton under the *HIL-locked* condition. The reason is that the shoulder horizontal flexion involves a more pronounced protraction/retraction of the scapula, giving rise to a considerable translation of the GH joint. Therefore, the GH joint deviated more from the baseline trajectory under the *HIL-locked* condition and demanded more compensatory trunk translation.

B. Assessment of the effects on muscle activations

The various test conditions primarily impacted the peak values of the EMG profiles. The statistical analysis verified the *transparency* of the robot in the *HIL-unlocked* condition, i.e., the EMG activity of the *HIL-unlocked* condition resembled that of the *baseline*. However, the PD muscle exhibited higher activation in the concentric phase during the sA/A frontal and sF/E horizontal movements. The increased muscle activation could be attributed to a reduced *transparency* of the shoulder powered joints due to dynamic disturbances (i.e., mechanical friction and inertia) that were not fully compensated by the low-level control. Including feedforward compensation of the friction and inertia of the actuation units is expected to reduce the EMG activity of the PD muscle.

In the case of sA/A frontal movement from the *HIL-unlocked* to the *HIL-locked*, the observed increased EMG activities of the TD and MD muscles can be explained by the inhibited scapulohumeral rhythm, which restricted shoulder abduction due to reduced vertical translation of the GH. To achieve a similar ROM as in the baseline test, arm abduction with the applied kinematic constraint during the HIL-locked condition induced higher EMG activation in the TD and MD muscles. However, no significant differences were observed for the sF/E sagittal movement, as this movement was not blocked.

Regarding the sF/E horizontal movement, a higher EMG activation of the MD muscle was found. This could be attributed to the significant trunk compensatory translation involved in the movement, inducing a trunk instability that requires increased isometric contraction of the MD muscles to stabilize the shoulder movement. Overall, while locking the passive DOFs significantly increased activations in specific muscles, comparable activations were observed with the passive DOFs unlocked, indicating the effectiveness of the exoskeleton's kinematic design in achieving proper kinematic compatibility.

C. Limitations of the study

Despite the clear patterns in the results, this study presents some limitations. First, we only evaluated the EMG activities on the shoulder muscles without considering the possible impact on the other muscles. Indeed, the lower back muscles could have been loaded to stabilize the trunk compensatory movement in the *HIL-locked* condition. Future investigations shall include this additional loading effect, together with the collection of participants' subjective feedback for a more comprehensive evaluation.

The average age of the participants was below that of the adult male population, as volunteers were young researchers. Considering the well documented age-related variations in shoulder functions [29], the inclusion of an age-matched sample is anticipated to mitigate the variability in the experimental results. Nonetheless, it would be interesting to investigate the self-aligning performance in an older population, despite the expected higher prevalence of pathology and past injuries in this cohort.

Finally, a non-randomized order of the conditions was chosen because a different order would have entailed a longer procedure for donning and doffing the exoskeleton, which could have negatively impacted the results. We acknowledge the potential for an order effect as subjects could become acclimated to the tasks across different conditions. Notably, the initial *HIL-unlocked* condition should have been more

susceptible to this effect. However, this limitation was mitigated by providing subjects adequate rest intervals between different test conditions to minimize possible biases from muscle fatigue. Additionally, participants were allowed to familiarize themselves with the tasks before data collection.

VI. Conclusion

This study presented the analysis of the kinematic compatibility of NESM-γ, an upper-limb exoskeleton designed for the rehabilitation training of stroke patients. The device integrated a mechanism for shoulder self-alignment made by passive joints to comply with natural movements of the shoulder complex and trunk. The experimental results showed that the proposed kinematic chain preserves the scapulohumeral rhythm and the natural GH joint movement patterns, keeping shoulder muscle activations close to the baseline. These patterns are significantly modified when the passive DOFs are locked, highlighting the need for kinematic solutions in shoulder exoskeletons that can accommodate the movements of the entire shoulder complex and trunk to achieve optimal kinematic compatibility. Future works with NESM-γ will focus on improving the low-level controllers to enhance the system's transparency, and the verification of the device in rehabilitation scenarios with post-stroke patients.

References

[1] H. Kobayashi, Y. Ishida, and H. Suzuki, "Realization of all motion for the upper limb by a muscle suit," in *RO-MAN 2004. 13th IEEE International Workshop on Robot and Human Interactive Communication (IEEE Catalog No.04TH8759)*, Sep. 2004, pp. 631–636. doi: 10/c7t5zb.

[2] C. O'Neill *et al.*, "Inflatable Soft Wearable Robot for Reducing Therapist Fatigue During Upper Extremity Rehabilitation in Severe Stroke," *IEEE Robot. Autom. Lett.*, vol. 5, no. 3, pp. 3899–3906, Jul. 2020, doi: 10/gngbgm.

[3] S. Lessard, P. Pansodtee, A. Robbins, J. M. Trombadore, S. Kurniawan, and M. Teodorescu, "A soft exosuit for flexible upper-extremity rehabilitation," *IEEE Trans. Neural Syst. Rehabil. Eng.*, vol. 26, no. 8, pp. 1604–1617, Aug. 2018, doi: 10/ghmtdc.

[4] N. Li *et al.*, "Bio-inspired upper limb soft exoskeleton to reduce stroke-induced complications," *Bioinspir. Biomim.*, vol. 13, no. 6, p. 066001, 2018, doi: 10/gngbdj.

[5] Q. Wu, B. Chen, and H. Wu, "Neural-network-enhanced torque estimation control of a soft wearable exoskeleton for elbow assistance," *Mechatronics*, vol. 63, p. 102279, Nov. 2019, doi: 10/gngbgn.

[6] A. H. A. Stienen, E. E. G. Hekman, F. C. T. van der Helm, and H. van der Kooij, "Self-Aligning Exoskeleton Axes Through Decoupling of Joint Rotations and Translations," *IEEE Transactions on Robotics*, vol. 25, no. 3, pp. 628–633, Jun. 2009, doi: 10/fft4tm.

[7] J. C. Perry, J. Rosen, and S. Burns, "Upper-limb powered exoskeleton design," *IEEE/ASME Transactions on Mechatronics*, vol. 12, no. 4, pp. 408–417, Aug. 2007, doi: 10/bgh5gk.

[8] H.-Y. Jang, Y.-H. Ji, J.-S. Han, A. M. Khan, J.-Y. Ahn, and C.-S. Han, "Development and verification of upper extremities wearable robots to aid muscular strength with the optimization of link parameters," *International Journal of Precision Engineering and Manufacturing*, vol. 16, no. 12, pp. 2569–2575, Nov. 2015, doi: 10/gngbg6.

[9] M. H. Rahman, M. J. Rahman, O. L. Cristobal, M. Saad, J. P. Kenné, and P. S. Archambault, "Development of a whole arm wearable robotic exoskeleton for rehabilitation and to assist upper limb movements," *Robotica*, vol. 33, no. 1, pp. 19–39, Jan. 2015, doi: 10.1017/S0263574714000034.

[10] X. Cui, W. Chen, X. Jin, and S. K. Agrawal, "Design of a 7-DOF cable-driven arm exoskeleton (CAREX-7) and a controller for dexterous motion training or assistance," *IEEE/ASME Transactions on Mechatronics*, vol. 22, no. 1, pp. 161–172, Feb. 2017, doi: 10/gngbfv.

[11] F. Xiao, Y. Gao, Y. Wang, Y. Zhu, and J. Zhao, "Design and evaluation of a 7-DOF cable-driven upper limb exoskeleton," *Journal of Mechanical Science and Technology*, vol. 32, no. 2, pp. 855–864, Feb. 2018, doi: 10/gc3zdt.

[12] A. Schiele and F. C. T. van der Helm, "Kinematic design to improve ergonomics in human machine interaction," *IEEE Transactions on Neural Systems and Rehabilitation Engineering*, vol. 14, no. 4, pp. 456–469, Dec. 2006, doi: 10/c9kbbw.

[13] D. Sui, J. Fan, H. Jin, X. Cai, J. Zhao, and Y. Zhu, "Design of a wearable upper-limb exoskeleton for activities assistance of daily living," in *2017 IEEE International Conference on Advanced Intelligent Mechatronics (AIM)*, in IEEE ASME International Conference on Advanced Intelligent Mechatronics. 345 E 47TH ST, NEW YORK, NY 10017 USA: IEEE, 2017, pp. 845–850.

[14] A. Zeiaee, R. Soltani-Zarrin, R. Langari, and R. Tafreshi, "Design and kinematic analysis of a novel upper limb exoskeleton for rehabilitation of stroke patients," in *2017 International Conference on Rehabilitation Robotics (ICORR)*, London: IEEE, Jul. 2017, pp. 759–764. doi: 10/gngbd4.

[15] B. Kim and A. D. Deshpande, "An upper-body rehabilitation exoskeleton harmony with an anatomical shoulder mechanism: design, modeling, control, and performance evaluation," *Int. J. Robot. Res.*, vol. 36, no. 4, pp. 414–435, Apr. 2017, doi: 10/gmbdnd.

[16] S. J. Ball, I. E. Brown, and S. H. Scott, "MEDARM: a rehabilitation robot with 5DOF at the shoulder complex," in *2007 IEEE/ASME international conference on advanced intelligent mechatronics*, Zurich, Switzerland: IEEE, 2007, pp. 1–6. doi: 10/czmknh.

[17] Y. Zimmermann, A. Forino, R. Riener, and M. Hutter, "ANYexo: A Versatile and Dynamic Upper-Limb Rehabilitation Robot," *IEEE Robot. Autom. Lett.*, vol. 4, no. 4, pp. 3649–3656, Oct. 2019, doi: 10/gh53ss.

[18] S.-H. Chen *et al.*, "Assistive control system for upper limb rehabilitation robot," *IEEE Trans. Neural Syst. Rehabil. Eng.*, vol. 24, no. 11, pp. 1199–1209, Nov. 2016, doi: 10/gjn3w7.

[19] L.-Q. Zhang, H.-S. Park, and Y. Ren, "Developing an intelligent robotic arm for stroke rehabilitation," in *2007 IEEE 10th International Conference on Rehabilitation Robotics*, Noordwijk, Netherlands: IEEE, Jun. 2007, pp. 984–993. doi: 10/bnpc34.

[20] E. Trigili *et al.*, "Design and Experimental Characterization of a Shoulder-Elbow Exoskeleton With Compliant Joints for Post-Stroke Rehabilitation," *IEEE/ASME Trans. Mechatron.*, vol. 24, no. 4, pp. 1485–1496, Aug. 2019, doi: 10/gngbch.

[21] A. Zeiaee, R. Soltani Zarrin, A. Eib, R. Langari, and R. Tafreshi, "CLEVERarm: A Lightweight and Compact Exoskeleton for Upper-limb Rehabilitation," *IEEE Robotics and Automation Letters*, pp. 1–1, 2021, doi: 10/gn34zv.

[22] A. Schiele, "Ergonomics of exoskeletons: Subjective performance metrics," in *2009 IEEE/RSJ International Conference on Intelligent Robots and Systems*, St. Louis, MO, USA: IEEE, Oct. 2009, pp. 480–485. doi: 10/dcgkvt.

[23] S. V. Sarkisian, M. K. Ishmael, and T. Lenzi, "Self-Aligning Mechanism Improves Comfort and Performance With a Powered Knee Exoskeleton," *IEEE Trans. Neural Syst. Rehabil. Eng.*, vol. 29, pp. 629–640, 2021, doi: 10/gk5shv.

[24] D. Park, S. Toxiri, G. Chini, C. D. Natali, D. G. Caldwell, and J. Ortiz, "Shoulder-Sidewinder (Shoulder-Side Wearable Industrial Ergonomic Robot): Design and Evaluation of Shoulder Wearable Robot With Mechanisms to Compensate for Joint Misalignment," *IEEE Trans. Robot.*, pp. 1–12, 2021, doi: 10/gnqxjs.

[25] J. Pan *et al.*, "NESM- γ: An Upper-limb Exoskeleton with Compliant Actuators for Clinical Deployment," *IEEE Robotics and Automation Letters*, pp. 1–8, 2022, doi: 10.1109/LRA.2022.3183926.

[26] T. Yoshikawa, "Manipulability of robotic mechanisms," *The International Journal of Robotics Research*, vol. 4, no. 2, pp. 3–9, 1985

[27] H. J. Hermens, B. Freriks, C. Disselhorst-Klug, and G. Rau, "Development of recommendations for SEMG sensors and sensor placement procedures," *J Electromyogr Kinesiol*, vol. 10, no. 5, pp. 361–374, Oct. 2000, doi: 10/fs7f65.

[28] C. J. W. Haarman, E. E. G. Hekman, J. S. Rietman, and H. van der Kooij, "Feasibility of reconstructing the glenohumeral center of rotation with a single camera setup," *Prosthetics and Orthotics International*, pp. 10–1097, Apr. 2022, doi: 10.1097/PXR.0000000000000132.

[29] C. W. Kolz *et al.*, "Age-related differences in humerothoracic, scapulothoracic, and glenohumeral kinematics during elevation and rotation motions," *J Biomech*, vol. 117, p. 110266, Mar. 2021, doi: 10.1016/j.jbiomech.2021.110266.